Journal of Cultural Heritage 75 (2025) 279–290

Contents lists available at ScienceDirect

Journal of Cultural Heritage

journal homepage: www.elsevier.com/locate/culher

Original article

Detecting pigments of cave paintings hidden beneath calcite layers: The potential of magnetic susceptibility and visible-to-infrared (400-2500 nm) reflectance spectroscopy

Morgane Jal[a,b,c,*], Christophe Durlet[b], Fabrice Monna[a], Chloé Morales[b,c], Franck Smektala[c], Carmela Chateau-Smith[b,d]

[a] ARTEHIS, UMR 6298, CNRS - Université Bourgogne Europe, 6 boulevard Gabriel, Dijon F-21000, France
[b] BGS – Biogéosciences, UMR 6282, CNRS - Université Bourgogne Europe, 6 boulevard Gabriel, Dijon F-21000, France
[c] INGEN Innovations Geosciences, 6 rue de Bastogne, Saint-Apollinaire F-21850, France
[d] CPTC, EA 4178, Université Bourgogne Europe, 4 boulevard Gabriel, Dijon F-21000, France

ARTICLE INFO

Article history:
Received 18 November 2024
Accepted 26 July 2025

Keywords:
Rock art
Magnetic susceptibility
Reflectance spectroscopy
Signal processing
Supervised classification
SWIR

ABSTRACT

Detecting cave paintings, protected but hidden beneath calcite layers, is an important step in completing the inventory of prehistoric art, yet it poses significant challenges. The mechanical removal of calcite is often invasive; image enhancement is often of limited effectiveness. This study investigates two non-invasive, complementary approaches to detect these hidden paintings: magnetic susceptibility and visible-to-infrared reflectance spectroscopy (400 to 2500 nm).

Reflectance measurements give detailed insights into pigment composition, while magnetic susceptibility measures the magnetic properties of materials and is particularly effective in detecting iron-based pigments such as hematite and goethite. The two methods were first tested in the laboratory on a limestone slab painted with various pigments and covered with calcite speleothem masks of varying thickness. This setup was a proxy for prehistoric cave paintings covered by opaque calcite speleothems. Both reflectance spectroscopy and magnetic susceptibility were used to assess pigment detectability. Results showed that magnetic susceptibility could detect iron-based pigments beneath thin calcite layers (up to 7 mm in laboratory conditions), while reflectance spectroscopy analysis identified the spectral differences between all the materials tested, although the signal decreased with speleothem thickness.

These findings were then validated in field tests at the Grande Grotte (Arcy-sur-Cure, France) where three prehistoric red ochre paintings covered by calcite were analysed. Both techniques were suitable for non-invasive detection: magnetic susceptibility was more effective for iron-based pigments, while reflectance spectroscopy provided broader mineralogical information.

While these methods are not yet fully operational for field use, this preliminary study shows that it should be possible to use both magnetic susceptibility and reflectance spectroscopy probes to detect and delineate paintings hidden (and protected) beneath opaque calcite layers.

1. Introduction

Prehistoric sites with cave paintings play a role in understanding the way of life and culture of ancient societies [1]. Preserving these sites and exploiting the knowledge they record is therefore essential. The first step before the analysis of rock paintings is obviously finding the figures, but this task can be quite challenging with the naked eye alone, especially when pigments have faded, or when they have been covered by layers of translucent-to-opaque calcite, forming speleothem coatings. These coatings may hide the artwork, but may also advantageously preserve the pigments from natural or anthropogenic degradation, as can be seen in the famous Caves of Altamira, Arcy-sur-Cure, Font-de-Gaume or Rouffignac [2–5], or the recent discovery of red clay-based paintings in Cova Dones [6].

Nowadays, two main approaches are used to find or to better distinguish hidden painted patterns in prehistoric caves and rock shelters. The first involves mechanically removing calcite layers (see works undertaken in the Kapova Cave in Russia [7] or in the Grande Grotte of Arcy-sur-Cure in France [8]). This method is

---

* Corresponding author at: ARTEHIS, UMR 6298, CNRS - Université Bourgogne Europe, 6 boulevard Gabriel, Dijon F-21000, France.
E-mail address: Morgane.Jal@ube.fr (M. Jal).

https://doi.org/10.1016/j.culher.2025.07.024

nonetheless invasive and time-consuming; worse still, it may lead to irreversible damage. Another approach uses the optical properties of the speleothem layer to visualize any hidden artwork. Most researchers process RGB images using a raster graphics editor to enhance the contrast between the painted figures and the background. More advanced techniques, involving the decorrelation and stretching of the RGB channels, possibly followed by changing the colour space, have met with great success within the archaeological community (see DStretch [9], and more recently, the ERA [10] software). To go beyond visible light (VIS, from 380 to 780 nm), researchers have first manipulated Near Infrared (NIR) imagery with the use of modified cameras (without IR cut filter) to detect reflective wavelengths up to 1100 nm. The NIR images sometimes reveal invisible pigments: under certain conditions, infrared light penetrates the calcite lattice more easily than visible light can [11]. The NIR technique, initially with film cameras [12], has been improved through increasingly efficient CCD and CMOS sensors [13]. Silicon-based photographic sensors are ineffective, however, for wavelengths greater than 1100 nm. Investigations at higher wavelengths, in the short-wave infrared range (SWIR, 1000–2500 nm), requires the use of specific sensors, for example based on InGaAs (indium gallium arsenide) components. Few studies have so far used SWIR sensors to detect rock art, providing convincing results for faded paintings [14,15], but to date, have not been applied to pigments masked below calcite layers. While hyperspectral analysis is routinely used in several fields of art history [16–19], it is only now beginning to be successfully applied to the study of cave paintings. Reflectance spectroscopy (RS) provides non-invasive access to the mineralogical and chemical composition of, across a broad range of wavelengths [20]. Other in situ spectrometric analytical techniques, such as spatially offset Raman spectroscopy (SORS) and portable X-ray fluorescence (pXRF), have also been successfully employed to study pigments in rock art [21–28]. To the best of our knowledge, these techniques have not yet been used in situ (i.e., within caves), specifically for detecting pigments covered by calcite layers. In this study, we test pXRF under laboratory conditions, but not SORS.

Magnetic susceptibility (MS), which measures the magnetization of material in response to an external magnetic field, may also detect masked iron-based pigments containing hematite or goethite [29]. The strong magnetic signal produced by such pigments might be measurable even beneath a few millimetres of diamagnetic calcite. Such a technique is routinely used in outdoor field archaeology to identify subsurface anomalies [30] but, to the best of our knowledge, it has so far been used only once to determine the origin of ochres in a rock art context [31].

2. Research aim

Our aim is to evaluate two methodological approaches using non-invasive RS (400–2500 nm) and MS analyses, both theoretically capable of detecting paintings hidden beneath translucent-to-opaque calcite layers of variable thickness. This work is structured in two parts: (*i*) a feasibility study to assess the performance of each method under controlled laboratory conditions; (*ii*) the application of the two techniques in a prehistoric cave, under authentic field conditions.

In the laboratory, a known amount of manganese, red ochre, yellow ochre, and charcoal (i.e. pigments commonly used in prehistoric paintings [5,32], as well as karstic sediment, was deposited on a limestone slab, serving as a proxy for a cave wall. Calcite masks of increasing thickness, crafted from natural speleothem, were then applied to simulate calcite layers. The RS and MS measurements were conducted both with and without these calcite masks to determine which pigments could be detected, to what extent, and with which thickness of calcite.

Subsequently, both methods were applied to three paintings from the famous Grande Grotte at Arcy-sur-Cure (Burgundy, France), a remarkable example of calcite precipitation covering ancient paintings. Our primary goals were thus to evaluate these methods in both controlled and field environments, and to identify the optimal conditions for their successful implementation in future research.

3. Materials and methods

3.1. Magnetic susceptibility (MS)

MS measurements (expressed in SI) were performed using a Magnetic Susceptibility Meter MS3, equipped with an MSK2 surface sensor, driven by Bartsoft software (all provided by Barting-

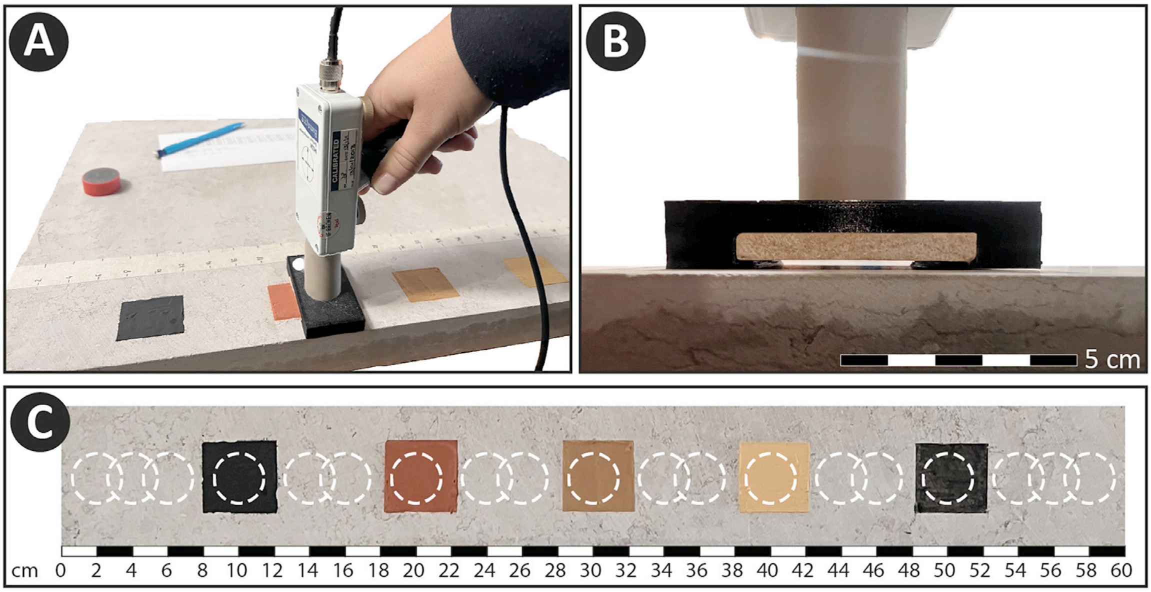

Fig. 1. Experimental setup for laboratory measurements. (A) Magnetic susceptibility measurement on the slab using the Surface Sensor (MSK2) from Bartington Instruments, designed to capture precise readings directly from the slab surface. (B) Close-up of the 3D-printed support structure for the sensor. This support prevents cross-contamination between measurement sites, while maintaining a consistent distance from the slab surface, ensuring reliable reproducible measurements. (C) Measurement profile on the slab. White dotted circles indicate measurement locations.

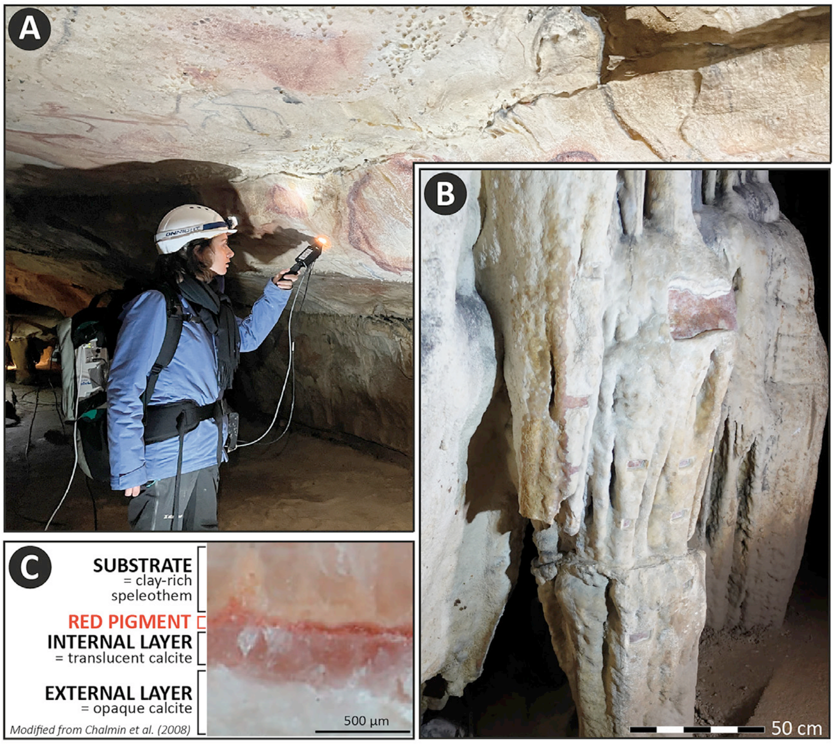

Fig. 2. Reflectance spectroscopy analysis of prehistoric pigments in the Arcy Cave. (A) Reflectance spectroscopy analysis using the ASD FieldSpec3 on the prehistoric paintings in the Salle des Vagues. (B) The Red Column, a stalagmite formation with zones of prehistoric red pigment application, now naturally coated by calcite layers of varying thickness (ranging from less than 1 mm to approximately 5 cm). Parts of the opaque calcite coating had been mechanically removed during previous studies. (C) Cross-section of an Arcy Cave stalactite showing red ochre covered by two calcite layers (modified after [32]).

ton Instruments; Fig. 1A). The surface area analysed was about 5 cm^2, with a full width at half maximum of 25.4 mm, as specified by the constructor [33]. The device was turned on at least 20 min before any measurements were taken. The integration time was set to 1 s. Potential drift was systematically corrected by bracketing each sample with two blanks, measured at more than 1 m away from any objects. A reference material provided by the manufacturer ($\chi = 430 \times 10^{-5}$ SI) was also measured at the beginning and end of each series to ensure accuracy. Our MS measurement was in very good agreement with the target value: $430 \times 10^{-5} \pm 2 \times 10^{-5}$ SI (1s).

3.2. Reflectance spectroscopy (RS)

The RS data were acquired using a FieldSpec 3 probe (Fig. 2A), operating with RS3 software (both from ASD Inc.). The probe has an approximate spot size of 10 mm in diameter. The device was turned on at least 30 min before any measurement, to prevent drift caused by heating. Prior to each measurement, the device was optimized by applying a proper dark current correction, and a white correction with a Spectralon panel, used as a white reference. Each measurement represents the average of 75 spectra collected at intervals of 0.2 s. As measurements are obtained by three different spectrometers, each with a specific wavelength range (350–1000 nm, 1000–1830 nm, and 1830–2500 nm), the resulting values exhibit steps at the splice of the three built-in detectors. A shift correction was therefore applied at 1000 nm and 1830 nm to maintain the continuity of the spectra [34,35]. The spectra were then normalized using their area under the curve, as generally recommended [36]. All data below 400 nm were discarded due to excessive noise, while the range from 400 to 2500 nm was smooth enough for noise filtering (e.g. Savitsky-Golay) to be unnecessary. The final spectra can be compared to the typical spectra of reference minerals and chemical compounds reported in various databases, including that of the USGS [37].

3.3. The laboratory experiment

3.3.1. Reproduction of natural field conditions

A limestone slab, 4 cm thick, measuring approximately 40 cm × 60 cm, was used to simulate a cave wall. It was chosen from a Comblanchien quarry in Burgundy, France, because of its textural homogeneity and its low insoluble residue content (Supp. Mat. 1). It is a bioturbated mudstone from a lagoonal environment of Bathonian age. Its elemental composition was semi-quantified, using a XRF spectrometer (Bruker S1 Titan LE), by referring to internal standards [38].

Various pigments often used in prehistoric times (manganese, red ochre, yellow ochre, and charcoal) were used as proxies for paintings (Supp. Mat. 2). Karstic sediment, consisting of clay-rich silts, were also added to this set, as they may naturally occur as decalcification products or endo-fluviatile inputs. The ochres and karstic sediment contain quartz and varying proportions of phyllosilicates (see Supp. Mat. 3). Red ochre is characterised by the presence of hematite, while goethite characterises yellow ochre. The manganese pigment consists of manganese oxides along with some aluminium oxides. The charcoal is a carbonized willow. The mineralogy of these materials was semi-quantitatively estimated using X-ray diffraction (D8 Endeavor, Bruker), following the protocol established by Holtzapffel (1985) [39]. All these analytical results, obtained from the GISMO analytical platform at the Bourgogne Europe University, are reported in supplementary materials (Supp. Mat. 1 & 3).

One gram of each of the four powdered pigments together with powered karstic sediment was diluted with distilled water and deposited directly on the slab to cover a ~16 cm^2 square. The five painted squares were separated by at least 6 cm of unpainted slab (Fig. 1).

Five calcite speleothem masks varying in thickness (2, 3, 4, 5, and 7 mm) were prepared from a large speleothem fragment

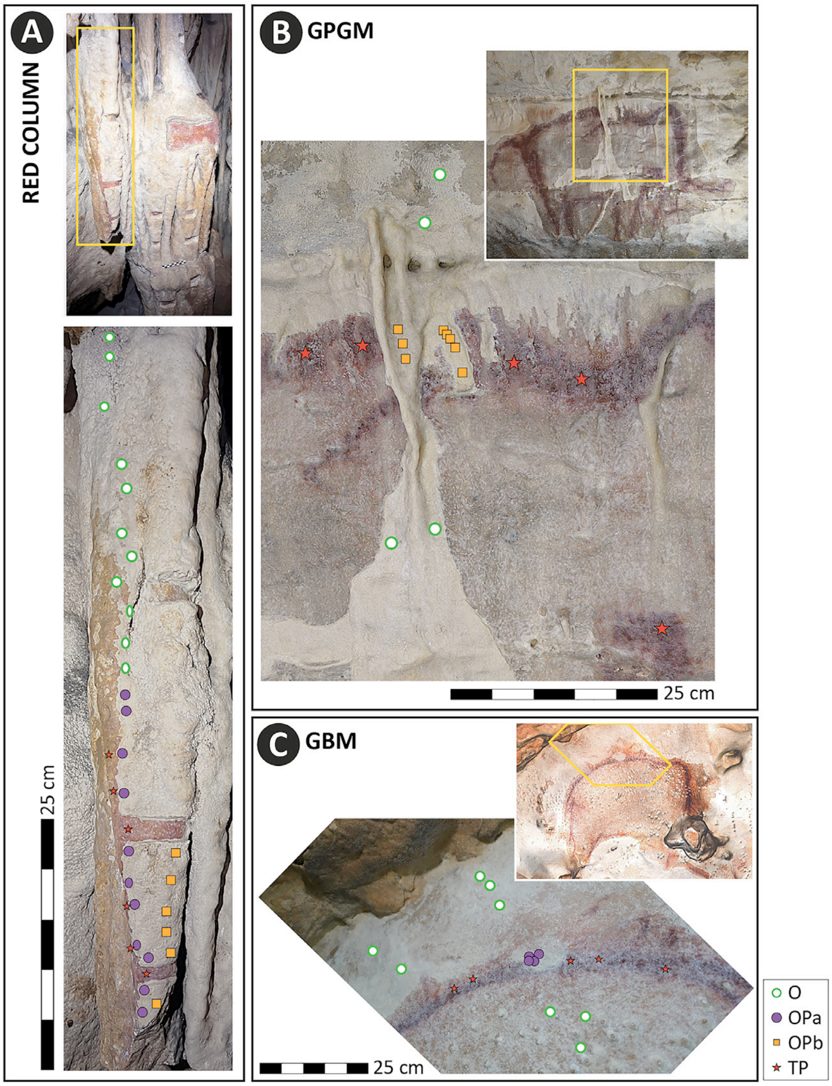

Fig. 3. Measurement locations and categories for both reflectance spectroscopy and magnetic susceptibility analyses in the Arcy Cave. The detailed location plan of the panels is provided in Supplementary Material 5. (A) Red Column, each magnetic susceptibility measurement point was measured several times to strengthen the dataset. (B) GPGM mammoth. (C) GBM mammoth.

fallen from a vertical wall in a Burgundy cave (Supp. Mat. 2). This speleothem is made up of alternating micritic and sparitic laminae, similar to the speleothems covering the Arcy Cave paintings [5,40], where sampling is strictly forbidden. Masks were sawn parallel to the laminae and then polished. The visual impact of applying them over pigments was evaluated using a VOLTCRAFT RGB-2000 colorimeter working in the visible spectrum (Supp. Mat. 4). Colours were characterised using standard D65 illuminant conditions in RGB and then converted to the CIELAB colour space (L*a*b*). This will allow the calculation of ΔE_{00}, a metric that quantifies the perceived difference between two colours (from 0 to 100). Note that $\Delta E_{00} > 3$ means a difference observable by the human eye [41]. Without any mask, differences between pigments and slab are clearly visible: ΔE_{00} between 10 and 43. Most of them are perceptible using the thinnest mask ($2.1 < \Delta E_{00} < 11.0$), but they can no longer be seen from the 4 mm mask onwards ($\Delta E_{00} < 3$).

3.3.2. Acquisition settings

To avoid the removal or cross-contamination of pigments during acquisition, probes and masks were attached to 3D-printed black nylon holders, each prepared to support either the probes alone or the probes plus a mask for each thickness (Fig. 1B). This set of holders ensured a consistent 1 mm gap between the pigments deposited on the slab and the bottom of the mask, or the probe alone for measurements without a mask.

For both RS and MS measurements, either with or without a mask, each series consists of five measurements in the centre of each of the 5 pigmented squares, together with 14 separate measurements of the raw slab (Fig. 1C). Unless otherwise specified, this protocol is replicated three times. Note that all measurements were taken in random order to mitigate any possible harmful effect of signal variation related to potential instrumental drift.

For the sake of completeness, it must be mentioned that pXRF was also tested. This attempt was unsuccessful: the pigment components became undistinguishable when a calcite mask was applied, even one as thin as 2 mm.

3.4. The Grande Grotte at Arcy-sur-Cure

The Grande Grotte at Arcy-sur-Cure, hereafter referred to as the Arcy Cave, is a fossil karstic conduit across a meander of the Cure River, developing in Oxfordian muddy limestone [42]. Some of the paintings here, mostly with hematite-rich red ochres (Fig. 2A), or more rarely with charcoal, have been dated to around 28 000 BP,

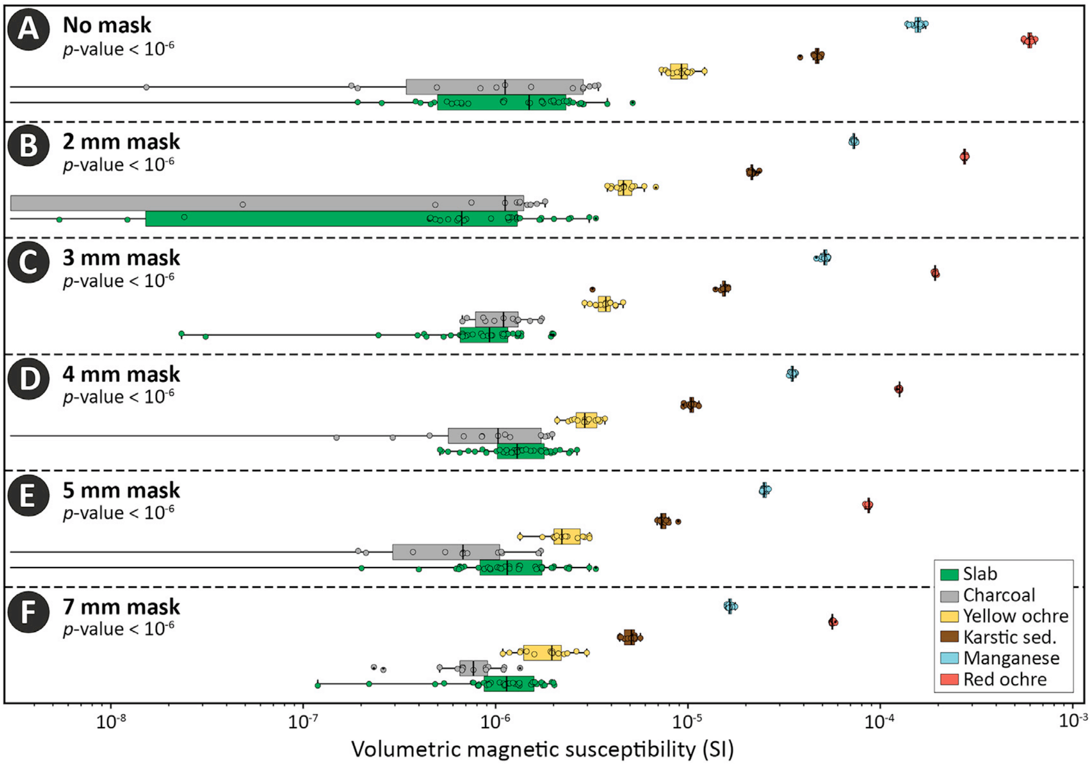

Fig. 4. Evolution of magnetic susceptibility for each of the pigments, karstic sediment and slab in relation to mask thickness, in the laboratory. (A) no mask, (B) 2 mm mask, (C) 3 mm mask, (D) 4 mm mask, (E) 5 mm mask, (F) 7 mm mask. Boxes display median, and first & third quartiles, whiskers show dispersion. The x-axis is logarithmic.

providing a unique insight into Palaeolithic art in the region [5 and references therein]. The Arcy Cave has drawn many visitors over the centuries, because of its accessibility, resulting in the accumulation of soot from torches and other lighting systems, darkening the walls. Aggressive cleaning with high-pressure water was undertaken in 1978 in the cave gallery open to tourist visits. It was not until 1990 that Pierre Guilloré detected paintings beneath the calcite layers that had preserved the pigments from destruction during wall cleaning [43]. As demonstrated by Chalmin and others [40], these wall speleothem coatings generally consist of two successive layers: (*i*) an external layer, up to 50 mm thick, composed of small whitish micritic calcite crystals, forming a shield that masks the pigments (Fig. 2B); (*ii*) an internal layer, from less than 1 mm to a few millimetres, with coarse translucent yellowish calcite crystals (sparite), protecting the pigments without concealing them (Fig. 2C). Archaeological surveys in this cave have so far led to the discovery of around 750 paintings and traces of pigments [5,44]. From 1997 to 2005, mechanical thinning with a dental drill removed the external layer of speleothem, but left the translucent internal layer to protect the paintings [5]. A few of these paintings still have small sections masked by the external layer of opaque calcite: three such sections were selected to assess the potential of RS and MS in field cave conditions (Fig. 3 and Supp. Mat. 5). The first target, the “Red Column” (Fig. 3A), was selected because exploratory rectangles micro-drilled through the external layer have revealed prehistoric red pigments masked by thin to thick opaque calcite layers (up to 50 mm thick) [5]. The remaining two targets, the “GPG mammoth” (GPGM, Fig. 3B) and the “GB mammoth” (GBM, Fig. 3C), were selected because an opaque calcite layer still covers part of the red pigment outlining the mammoth’s back on each panel.

Four classes of measurement points were then defined:

- O: thick or thin opaque speleothem (up to 50 mm thick) with no pigment underneath,
- OPa: thick opaque speleothem (> 3 mm) masking red pigment,
- OPb: thin opaque speleothem (< 3 mm) masking red pigment,
- TP: thin translucent speleothem (less than 2 mm) covering red pigment without masking it.

The sampling points (used for both MS and RS measurements) were selected to ensure that all four classes were sufficiently represented (Fig. 3).

3.5. Statistical processing

The MS values resulting from both laboratory acquisition and field measurement were sorted into the relevant number of classes. The statistical treatment was therefore a simple univariate comparison of more than two independent classes of equal or different sample sizes. As the number of samples composing the classes was often low, with no prior assumption about distribution, a non-parametric Kruskal-Wallis test was used to assess whether all the samples were from the same population, or whether at least one class was from a different population. If so, Dwass-Steel-Critchlow-Fligner (DSCF) pairwise comparisons were used as a post-hoc test [45].

Comparing classes of RS data is much more challenging: (*i*) the problem is highly multivariate; (*ii*) neighbouring variables (in terms of wavelengths) show strong intercorrelations; (*iii*) variables are much more numerous than observations. To address this issue, methods based on Partial Least Squares (PLS) are frequently applied in chemometrics because of their effectiveness, more particularly when RS data are involved [46–51]. A PLS regression first constructs latent variables to maximize the covariance between predictor variables and categorical response variables (classes), each considered as a block of variables. It then selects the best number of components (i.e. latent variables) to approximate the original variable space, while retaining the greatest proportion of the total variance expressed. This step vastly reduces dimensionality.

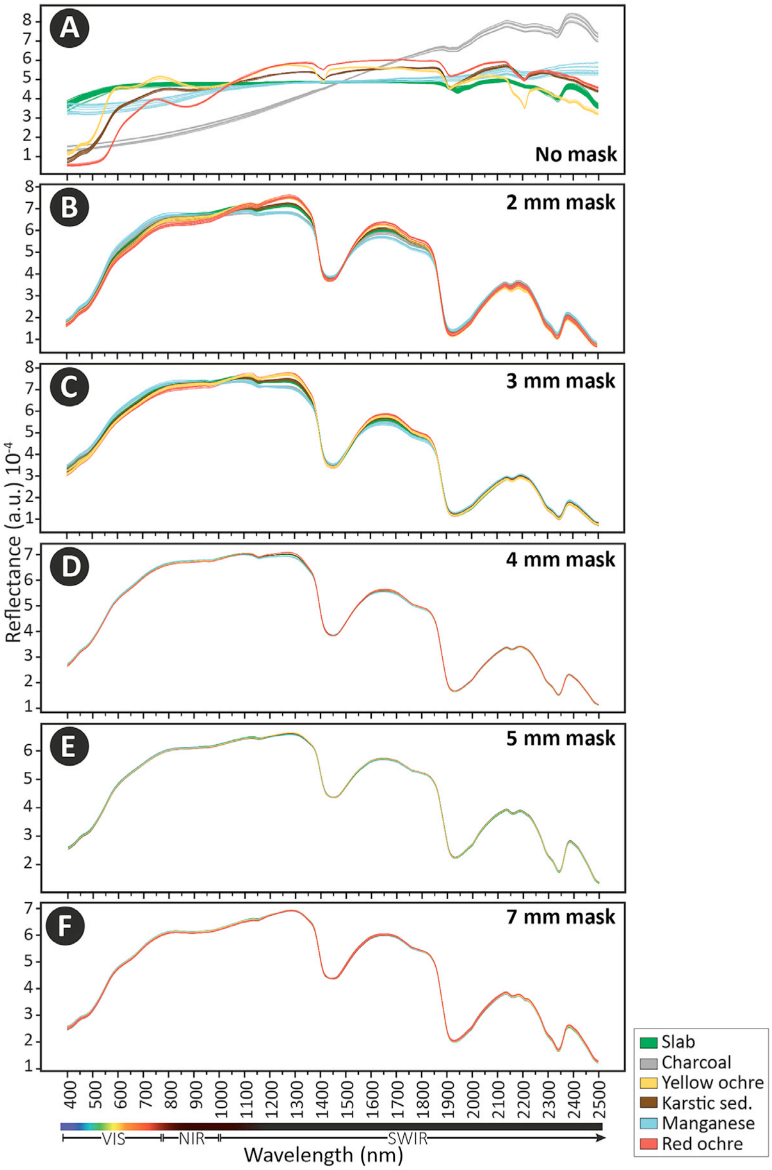

Fig. 5. Reflectance spectra of the pigments, karstic sediment and slab in relation to mask thickness, in the laboratory. (A) no mask, (B) 2 mm mask, (C) 3 mm mask, (D) 4 mm mask, (E) 5 mm mask, (F) 7 mm mask. VIS: visible region. NIR: near infrared region. SWIR: short-wave infrared region. a.u.: arbitrary units.

At this point, the scores of latent variables can be used as input features in classification models.

In this study, two different supervised machine learning algorithms for classification were applied, with from 2 to 7 latent variables included in the model. The first is the Discriminant Analysis (DA), which aims at finding the best linear combination of variables to separate the classes. This method, often associated with PLS [52–54], is widely discussed in the literature, generally as PLS-DA [55]. The second is the Random Forest (RF) algorithm, a more recent method that belongs to ensemble learning methods for classification. It has also sometimes been used in combination with PLS [56,57], here termed as PLS-RF. The algorithm works by aggregating multiple randomly constructed classification trees. Instead of selecting splits based on feature importance, the best feature is chosen from a random subset of input variables. The principle behind the algorithm is that individual decision trees may make incorrect predictions, but their label predictions become more correct and stable when combined. Compared to DA, RF presents the advantage of handling cases where decision boundaries can be both linear and non-linear. This method has already been successfully applied in the context of both spectral and hyperspectral data [47,50,58].

One way of evaluating the capacity of the models produced to generalize and accurately predict the classes is to divide the data into a training set and a validation set. It is even more effective to use three sets: training, validation, and test. In this study, given the limited number of spectra, a Leave-One-Out Cross-Validation approach was preferred. Each spectrum was sequentially used for evaluation, with the other spectra used for training. All predictions are then combined to calculate performance metrics. The accuracy score measures how often the model predictions match the true labels. This commonly used metric is, however, prone to fail when dealing with imbalanced classes [59]. This scenario is even more applicable to the laboratory experiment, where there are 3 times more measurements for the raw slab than for each of the pigments. The F1-score avoids these drawbacks, by combining precision and recall (Eq. (1)).

$$\mathrm{F1-score} = \frac{TP}{TP + \frac{1}{2}(FN + FP)}, \tag{1}$$

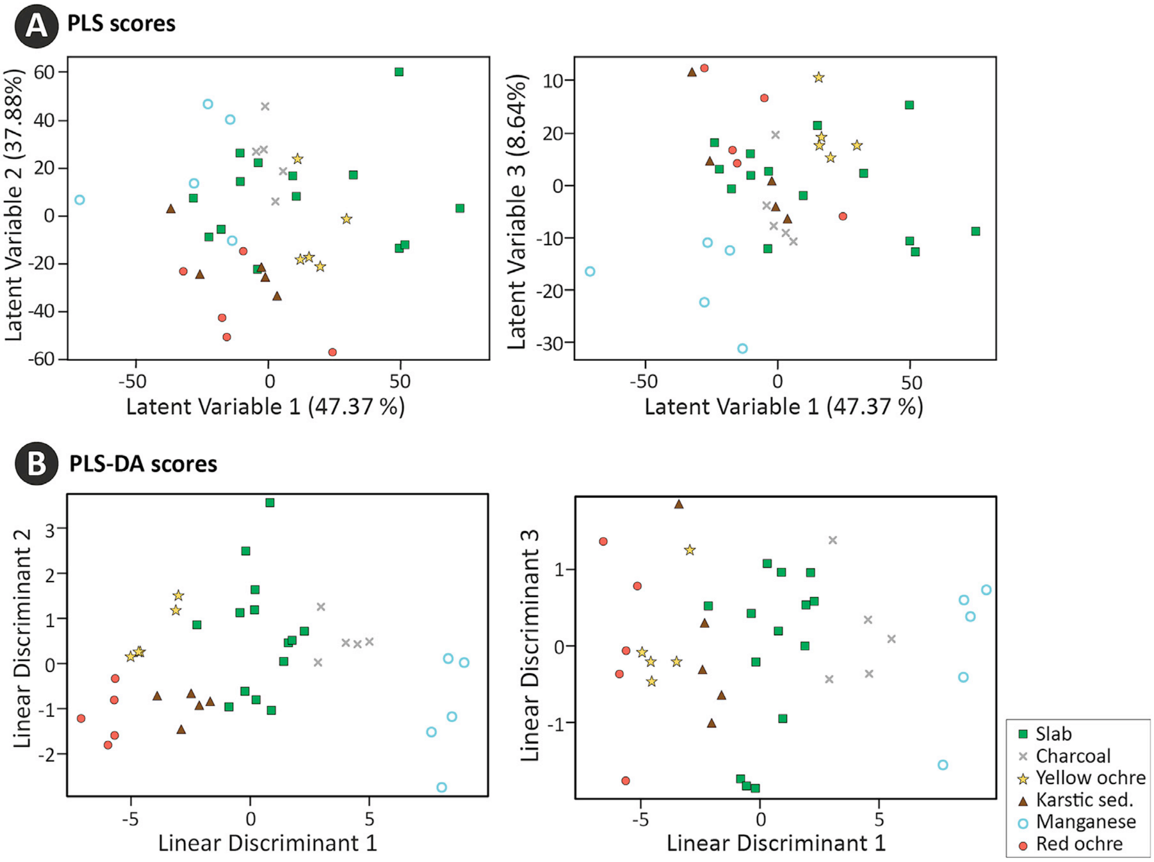

Fig. 6. Multivariate analysis of the 6 materials for PLS and PLS-DA with a 4 mm mask and an optimized number of components ($n = 3$), in the laboratory. (A) Partial Least Squares (PLS) scores plots showing the distribution of samples based on latent variables. (B) Partial Least Squares Discriminant Analysis (PLS-DA) scores plots illustrating the separation of samples according to Linear Discriminants.

where TP corresponds to True Positives, FP to False Positives, TN to True Negatives, and FN to False Negatives. The F1-score was thus chosen as the main metric, but accuracy together with precision and recall are also reported for information (see [60] for more details about the computation of these metrics).

To determine the relative importance of spectral variables in detecting pigments, five PLS models were built for each pigment vs. slab. Then, the VIP scores (VIP for Variable Importance in Projection) [61–64] were computed [65]. These scores are computed as the weighted sum of the squared PLS weights, where the weights are proportional to the amount of variance explained in the dependent variable by each latent component. Wavelengths presenting VIP scores above 1 are generally considered as relevant [63,66].

Data processing, statistical inferences, and machine learning were scripted in Python 3.11, using the relevant libraries (i.e. Pandas, NumPy, Matplotlib, and Scikit-learn).

4. Results and discussion

4.1. Laboratory experiment

4.1.1. Magnetic susceptibility

The median MS values (in SI) ranged from $\sim 10^{-6}$ for raw slab and charcoal to $\sim 6 \times 10^{-4}$ for red ochre (Fig. 4). The values were always ranked in the same order: red ochre > manganese > karstic sediment > yellow ochre. These signals attenuate exponentially as mask thickness increases, whereas the values for raw slab and charcoal remain steady throughout the experiment (Fig. 4A-F). More formally, the p-value of the Kruskal-Wallis test was $<10^{-6}$, indicating that the existence of differences between at least two classes is statistically confirmed. After post-hoc DSCF pairwise comparisons, red ochre, manganese, karstic sediment, and yellow ochre were significantly different from each other (p-value $<10^{-3}$, Supp. Mat. 6a). By contrast, raw slab and charcoal could never be statistically distinguished by MS, except with the 7 mm mask (p-value $= 0.022$).

As expected, the contrast between the raw slab and the pigmented areas was greatest when no mask was present (Fig. 4A). The observed variations in MS among the materials can be attributed to their specific mineralogical composition, which governs their magnetic characteristics [67]. Due to their high hematite content, red ochre and manganese produce higher magnetic signals than yellow ochre and karstic sediment, which are composed in part of goethite and variable amounts of phyllosilicates. Although these minerals are known to be magnetic, they are much less so than hematite [67]. By contrast, the MS of charcoal obtained from carbonized willow is negligible, consistent with the non-magnetic nature of this carbonaceous material. The MS differences observed between slab and charcoal, both under a 7 mm-mask, are counter-intuitive and not understood currently.

To summarize, MS appears to be an efficient tool for discovering red paintings masked by calcite, at least under laboratory conditions.

4.1.2. Reflectance spectroscopy

As expected, in the absence of a calcite mask, the set of spectra was visibly different for each material, because of their great variety in both colour and mineralogical composition (Fig. 5A). The differences between the normalized reflectance spectra faded quickly once a calcite mask was applied (Fig. 5B-F; see Supp. Mat. 7 for

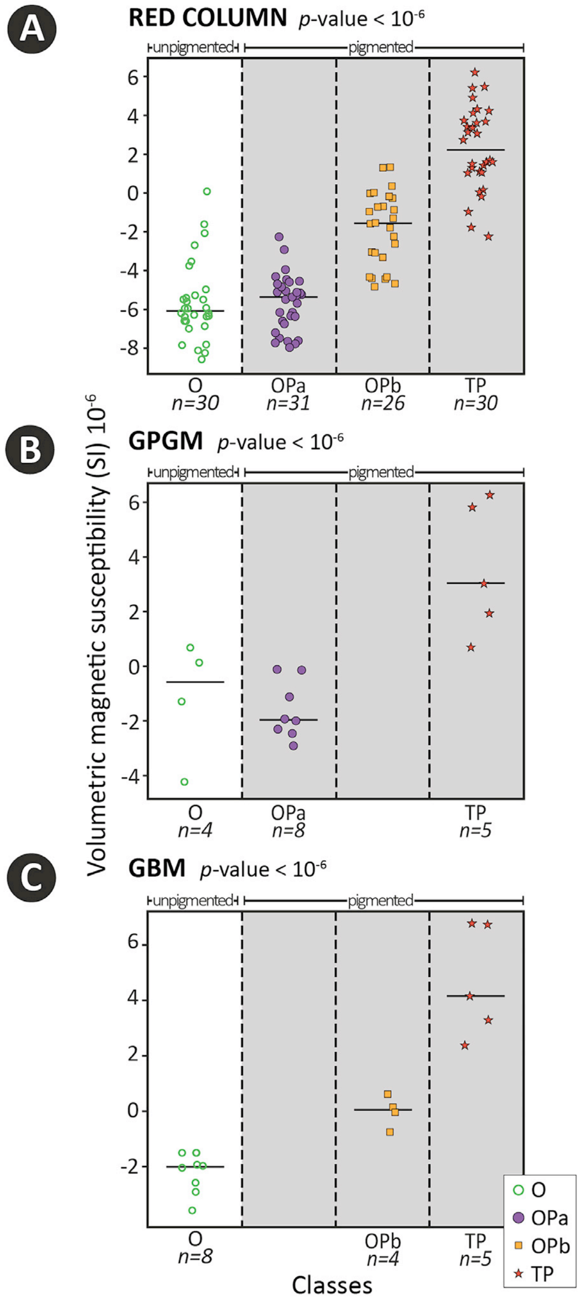

Fig. 7. Evolution of magnetic susceptibility for different classes at Arcy Cave. Sample sizes (n) are indicated below each group. Horizontal black lines represent the median value for each group. (A) Magnetic susceptibility measurements for the Red Column, where all four classes are present (O, OPb, OPa, and TP). (B) Magnetic susceptibility measurements for the GPGM mammoth, where only three classes are present (O, OPa, and TP). (C) Magnetic susceptibility measurements for the GBM mammoth, where only three classes are present (O, OPb, and TP).

larger figures, each set of spectra is shown on a full page with an offset to enhance visualization). With masks, the RS signal is driven by the calcite spectral signature (See carbonate absorption bands in Supp. Mat. 8). Nevertheless, slight differences, more indicative of intensity levels than distinct spectral features, remained visible with the 2 mm and 3 mm masks (Fig. 5B-F). A series of statistical analyses was then applied to classify the data.

The analyses for the 4 mm mask are presented in Fig. 6 for purposes of illustration. Fig. 6A presents the sample scores for the three latent variables obtained with the PLS model, which together account for 93.89 % of the total variance. With this method, some organisation can be perceived, but intermixing is also present. The slab samples are the most randomly distributed, spreading all over the point cloud. Adding DA to PLS clarifies the situation (Fig. 6B). The 6 classes are well delineated, and the LD1 axis is highly discriminant. As a result, the F1-score (like the other metrics) is perfect, with a value of 1 (like with a mask thinner than 4 mm, given that the number of components is optimized and the best model selected). The discrimination between classes with PLS-DA is nearly perfect, at least up to the 5 mm mask (F1-score = 0.974 -Table 1; see also the other metrics in Supp. Mat. 10). With the 7 mm mask, PLS-RF performs better than PLS-DA, however the F1-score decreases to 0.5, while the number of latent variables necessary to optimize the model increases, due to the increasing complexity of the problem at hand (See Table 1). In all cases, differences between classes are significant, and the ability of the models to predict classes is much better than random chance (see *p*-value in Table 1).

To summarize, the statistical analyses applied here result in an efficient classification of the spectral data, ultimately enhancing the accuracy of pigment detection and differentiation. At this point, a question is raised: what are the spectral regions that contribute the most to the discrimination model, and this for each of the pigments compared to the slab? Without masks, the VIP scores (Supp. Mat. 8) unsurprisingly confirm that the visible range (up to about 800 nm) is the most important for differentiating between pigments and slab. Wavelengths of interest also emerge in the SWIR region, particularly beyond 2350 nm, a region known for combination and overtone bands involving OH groups and/or carbonate ions (CO_3^{2-}). For red ochre, karstic sediment, and yellow ochre, another region around 1200–1300 nm appears relevant, but is absent for manganese and charcoal pigments. For more details, the reader can refer to Supp. Mat. 8 and 9, which report specific absorption bands and spectral interpretations [73–82]. Note that the absorption band associated with Fe electronic transitions, near 860 and 900 nm, does not significantly contribute to distinguishing the slab from the pigments with high iron content — a counter-intuitive result given the substantial iron content of these materials. Certain characteristic spectral positions associated with the presence of elements or minerals typical of our pigments (e.g. Fe electronic transitions - the bands around 860 and 900 nm related to iron; OH combination bands - the distinctive kaolinite doublets near 1400 nm and 2200 nm; CO_3^{2-} combination bands - the carbonate-associated band around 2330 nm) were no longer visible once the mask was applied. The VIP scores then no longer highlighted spectral regions specific to each material (example provided for a 4 mm-mask in Supp. Mat. 8), as almost the entire spectrum appears to contribute to the discrimination, but with higher VIP scores below 1400 nm than above 1500 nm, in the SWIR. The narrow band around 1400–1500 nm consistently lacks significance, regardless of the material. It corresponds to a combination band involving either OH vibrations or H_2O vibrations.

The fact that almost the entire spectrum carries information relevant to the discrimination of hidden pigments fully justifies the use of statistical techniques that consider the entire spectral range, rather than selecting only a few supposedly relevant spectral regions to build a supervised classification model.

4.2. Arcy-sur-Cure measurements

4.2.1. Magnetic susceptibility

The MS measurements of the three panels studied (i.e., Red Column, GPGM and GBM mammoths) are reported in Fig. 7. The four previously defined classes are organised from left to right as follows: opaque calcite with no pigment underneath (O), thick calcite covering pigment (OPa), thin calcite covering pigment (OPb), and transparent calcite with visible pigment (TP). Note that the

Table 1
Optimal model and performance: laboratory experiment (6 mask thicknesses); Arcy cave (3 panels). PLS: Partial Least Squares. DA: Discriminant Analysis. RF: Random Forest. Number of components equals number of latent variables. For F1-score details, see Eq. (1). The *p*-values above 10^{-2} indicate that model prediction is better than random chance. *Only one series was acquired (instead of three).

		Model	Number of components	F1-score	*p*-value
LABORATORY EXPERIMENT	Without mask	PLS-DA	2	1	$< 10^{-6}$
	With 2 mm mask	PLS-DA	3	1	$< 10^{-6}$
	With 3 mm mask	PLS-DA	2	1	$< 10^{-7}$
	With 4 mm mask*	PLS-DA	3	1	$< 10^{-3}$
	With 5 mm mask*	PLS-DA	6	0.974	$< 10^{-4}$
	With 7 mm mask	PLS-RF	7	0.500	$< 10^{-5}$
ARCY CAVE	Red Column	PLS-RF	2	1	$< 10^{-6}$
	GPGM mammoth	PLS-DA	4	1	$< 10^{-4}$
	GBM mammoth	PLS-DA	7	1	$< 10^{-5}$

signal dynamics observed in field conditions are lower than those recorded in the laboratory, probably because a larger amount of pigment was deposited on the slab compared to what was used on the cave walls by our ancestors.

As the three paintings are associated with two different substrates (calcite speleothem or Jurassic limestone), the MS values for O range approximately from -6×10^{-6} for the Red Column to -0.5×10^{-6} for the GPGM mammoth (Fig. 7). The detection of paintings is expected to improve when the MS signal of the unpainted cave wall remains relatively steady and low compared to that of the painted areas. Such conditions should enhance the signal-to-noise ratio. The Kruskal-Wallis tests indicate that there are always significant differences between two or more classes whatever the targeted panel (p-values $< 10^{-6}$), justifying the application of post-hoc DSCF pairwise comparisons (Supp. Mat. 6b). No statistical difference can be observed between O and OPa, indicating that, under a thick layer of calcite (> 3 mm), the contrast between MS signals is too low to be significant. By contrast, the MS signals for OPb are greater than either O or OPa, while the MS signals for TP are always the highest. This is consistent with lab results showing reduced pigment detection as the calcite layer becomes thicker. MS is confirmed as an efficient tool for the three targets studied, though the small quantity of ochre (or its preservation) limits this approach when the calcite layer is too thick, or the limestone substrate is iron-rich.

4.2.2. Reflectance spectroscopy

The spectra acquired for the Red Column, the GPGM and the GBM mammoths panels are presented in Fig. 8 and Supp. Mat 11. At first glance, they share common patterns with those obtained using calcite masks during the laboratory experiment. Slight differences are nonetheless noticed especially in the VIS region and around 1450 nm and 1950 nm (Fig. 8, see also Supp. Mat. 9 and Supp. Mat. 12 for detailed absorption features). Such variations may arise from differences in OH bending vibrations related to relative humidity [68–70], as laboratory conditions are dry, whereas the cave walls are often quite wet. Another possibility is the differences in the crystallinity, texture, and geochemical composition of the calcite, i.e. masks and internal/external layers in the Arcy Cave (Fig. 1C). All spectra corresponding to visible red pigment (TP) show absorption bands around 850–910 nm indicating the presence of iron in the form of hematite and/or goethite [68,71,72].

Both PLS-DA and PLS-RF, with from 2 to 7 components, were tested on the three panels (Supp. Mat. 13), considering 4 classes for

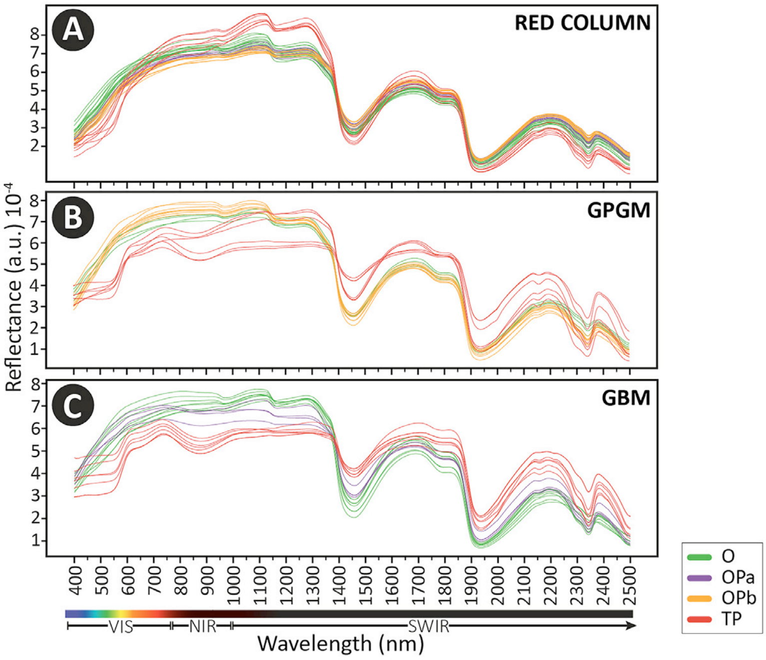

Fig. 8. Reflectance spectra for different classes at Arcy Cave. VIS: visible region. NIR: near infrared region. SWIR: short-wave infrared region. a.u.: arbitrary units. (A) Reflectance spectra for the Red Column, where all four classes are present (O, OPa, OPb, TP). (B) Reflectance spectra for the GPGM mammoth, where only three classes are present (O, OPa, TP). (C) Reflectance spectra for the GBM mammoth, where only three classes are present (O, OPb, TP).

the Red Column, and 3 classes for the two mammoths. When the best model is selected (Table 1), perfect discrimination is reached (F1-score = 1), demonstrating that properly processed RS analyses can detect hidden red pigments, even beneath an opaque speleothem layer more than 3 mm thick (Table 1, see also Fig. 8 for spectra).

5. Conclusion

This study demonstrates that magnetic susceptibility and visible-to-infrared reflectance spectroscopy analysis are effective tools for detecting prehistoric paintings hidden beneath calcite layers. MS is particularly effective in detecting iron-based pigments like hematite and goethite, while RS analysis relies more on mineralogical contrast. Both methods are non-invasive, thus preserving the integrity of archaeological artefacts. Although the thickness of the calcite layer does affect results to some extent, pigments that are completely invisible to the naked eye can still be detected by MS and RS at least to a thickness of 3 mm in the field and 7 mm in the laboratory.

For the sake of completeness, the methods presented here should not be considered, at least for the moment, as an operational solution, but rather as proof of concept. If the results obtained here are so impressive, it is because we have studied an almost ideal situation where models could be produced under supervision. The reality of working on a new site is much more challenging, as the paintings are not known beforehand and must be discovered. Substantial variations in the amount of pigment applied (or preserved) may introduce noise. In addition, environmental factors, such as variable surface moisture and heterogeneity of the substrate in terms of thickness and composition, can also make point-to-point comparison of results more difficult. As a result, the models produced are probably not generalizable, necessitating a less efficient approach based on unsupervised classification. This study thus emphasizes the importance of adapting these techniques to a variety of natural conditions, possibly by combining both MS and RS measurements to establish the models, instead of processing each feature separately.

Looking ahead, by integrating a hyperspectral data cube (acquired from a VIS+NIR+SWIR camera rather than solely from an RS sensor as in the present study) with real-time data processing, researchers can envision a future where pigments are detected directly through cave wall scans. For MS, implementation in the field is time-consuming, as it requires a large set of measurements, at high spatial resolution, with at least some arbitrary spatial reference. Combining the MS sensor with inertial measurement units could notably accelerate the process. Although still in their infancy for parietal art, the approaches discussed here, possibly in combination, may facilitate the efficient mapping and analysis of prehistoric parietal art, offering new perspectives for archaeological research.

Funding sources

This research was supported by a CIFRE agreement [2021/1383] and fundings provided by the ARTEHIS - UMR 6298, and Biogéosciences - UMR 6282 laboratories.

Acknowledgements

We would like to express our heartfelt thanks to François and Emmanuel De la Varende, the owners and operators of the Arcy Caves, for granting permission for investigations in the Grande Grotte. Our gratitude also goes to the welcoming team and guides for their support during our stay. Special thanks to Yves Pautrat for facilitating our connection and the initiation of the relevant administrative procedures, as well as to the agents of the SRA BFC for their oversight of the project. Our study has greatly benefited from the extensive rock art research conducted by specialists in the Arcy Cave [5] prior to our study. We thank INRAE Bourgogne-Franche-Comté for lending the reflectance spectroscopy probe, particularly Stéphane Follain and Jean-Benoît Masson. Our thanks also go to Olivier Musset for his help during field acquisitions and subsequent discussions, as well as Ludovic Bruneau for his assistance in the field and for the analyses conducted at the GISMO platform. We acknowledge INGEN: Innovation Geosciences for their material support, especially Julie Suzialuk for her assistance in the field, as well as Philippe Blanc from LITHOLOGIE BOURGOGNE for his help and material support in the preparation of calcite masks used during laboratory analyses. We are grateful for comments by the anonymous reviewers and the editor, which have greatly improved the manuscript.

Supplementary materials

Supplementary material associated with this article can be found, in the online version, at doi:10.1016/j.culher.2025.07.024.

References

[1] A. Schnapp, S.H. Aufrère, F. Baratte, F. Coarelli, Préhistoire Et Antiquité : Des Origines De L'humanité Au Monde Classique, Flammarion, Paris, France, 2011.
[2] F. Plassard, Les grottes ornées de Combarelles, Font-de-Gaume, Bernifal, et Rouffignac. Contexte archéologique, thèmes et style des représentations., PhD thesis, Université Sciences et Technologies - Bordeaux I, 2005.
[3] V. Jurado, A. Fernandez-Cortes, S. Cuezva, L. Laiz, J. Cañaveras, S. Sanchez-Moral, C. Saiz-Jimenez, The fungal colonisation of rock-art caves: experimental evidence, Naturwissenschaften 96 (2009) 1027–1034, doi:10.1007/s00114-009-0561-6.
[4] F. Plassard, B. Kervazo, C. Ferrier, I. Reiche, S. Konik, J. Castaing, H. Rousselière, N. Aujoulat, Altérations et dépôts sur les parois de la grotte de Rouffignac : premiers résultats d'analyses, PALEO Rev. Archéol. Préhist. (2014).
[5] D. Baffier, E. Bertin, M. Guirard, E. Guillamet, La Grande Grotte d'Arcy-Sur-Cure (Yonne), EUD, Dijon, 2024.
[6] A. Ruiz-Redondo, V. Barciela, X. Martorell, Cova Dones: a major Palaeolithic cave art site in eastern Iberia, Antiquity (2023) 1–5, doi:10.15184/aqy.2023.133.
[7] E. Devlet, E. Guillamet, A. Pakhunov, N. Grigoriev, D. Gainullin, The camel in the cave ice age art in the Ural mountains, World Archaeol. (2018) 10–11.
[8] M. Girard, D. Baffier, J. Brunet, E. Guillamet, L'intervention directe sur les parois: un apport à la connaissance des tracés préhistoriques : le cas de la Grande Grotte d'Arcy-sur-Cure, in: Art Avant Hist. Conserv. Art Préhistorique, SFIIC, Paris, 2002, pp. 197–208.
[9] J. Harman, DStretch Algorithm Description, (2008).
[10] F. Monna, T. Rolland, J. Magail, Y. Esin, B. Bohard, A.C. Allard, J. Wilczek, C. Chateau-Smith, ERA: a new, fast, machine learning-based software to document rock paintings, J. Cult. Herit. 58 (2022) 91, doi:10.1016/j.culher.2022.09.018.
[11] M.D. Lane, Midinfrared optical constants of calcite and their relationship to particle size effects in thermal emission spectra of granular calcite, J. Geophys. Res. Planets 104 (1999) 14099–14108, doi:10.1029/1999JE900025.
[12] G. Fredlund, L. Sundstrom, Digital infra-red photography for recording painted rock art, Antiquity 81 (2007) 733–742, doi:10.1017/S0003598X00095697.
[13] H. Helmers, M. Schellenberg, CMOS vs. CCD sensors in speckle interferometry, Opt. Laser Technol. 35 (2003) 587–595, doi:10.1016/S0030-3992(03)00078-1.
[14] V. Bayarri, E. Castillo, S. Ripoll, M.A. Sebastián, Improved application of hyperspectral analysis to rock art panels from El Castillo Cave (Spain), Appl. Sci. 11 (2021) 1292, doi:10.3390/app11031292.
[15] B. Schmitt, Z. Souidi, F. Duquesnoy, F.V. Donzé, From RGB camera to hyperspectral imaging: a breakthrough in Neolithic rock painting analysis, (2023). 10.21203/rs.3.rs-2149396/v1.
[16] F. Daniel, A. Mounier, J. Pérez-Arantegui, C. Pardos, N. Prieto-Taboada, S. Fdez-Ortiz de Vallejuelo, K. Castro, Hyperspectral imaging applied to the analysis of Goya paintings in the Museum of Zaragoza (Spain), Microchem. J. 126 (2016) 113–120, doi:10.1016/j.microc.2015.11.044.
[17] A. Candeo, B. Ardini, M. Ghirardello, G. Valentini, L. Clivet, C. Maury, T. Calligaro, C. Manzoni, D. Comelli, Performances of a portable Fourier transform hyperspectral imaging camera for rapid investigation of paintings, Eur. Phys. J. Plus 137 (2022) 409, doi:10.1140/epjp/s13360-022-02598-7.
[18] C. Mecquenem, M. Eveno, M. Alfeld, R. Pillay, E. Laval, E. Ravaud, I. Reiche, A multimodal study of smalt preservation and degradation on the painting "Woman doing a Libation or Artemisia" from an anonymous painter of the Fontainebleau School, Eur. Phys. J. Plus 138 (2023) 185, doi:10.1140/epjp/s13360-023-03799-4.

[19] R. Pillay, J.Y. Hardeberg, S. George, Hyperspectral imaging of art: acquisition and calibration workflows, J. Am. Inst. Conserv. 58 (2019) 3–15, doi:10.1080/01971360.2018.1549919.

[20] F.A. Kruse, Mapping surface mineralogy using imaging spectrometry, Geomorphology 137 (2012) 41–56, doi:10.1016/j.geomorph.2010.09.032.

[21] M. Gay, K. Müller, F. Plassard, J.J. Cleyet-Merle, P. Arias, R. Ontañón, I. Reiche, Efficient quantification procedures for data evaluation of portable X-ray fluorescence – Potential improvements for Palaeolithic cave art knowledge, J. Archaeol. Sci. Rep. 10 (2016) 878–886, doi:10.1016/j.jasrep.2016.06.008.

[22] P. Vandenabeele, A. Rousaki, Developing macro-raman mapping as a tool for studying the pigment distribution of art objects, Anal. Chem. 93 (2021) 15390–15400, doi:10.1021/acs.analchem.1c03197.

[23] S. Moyo, D. Mphuthi, E. Cukrowska, C. Henshilwood, K. Niekerk, L. Chimuka, Blombos Cave: middle Stone Age ochre differentiation through FTIR, ICP OES, ED XRF and XRD, Quat. Int. 404 (2016) 20–29, doi:10.1016/J.QUAINT.2015.09.041.

[24] M. Realini, C. Conti, A. Botteon, C. Colombo, P. Matousek, Development of a full micro-scale spatially offset Raman spectroscopy prototype as a portable analytical tool, Analyst 142 (2) (2017) 351–355, doi:10.1039/c6an02470j.

[25] M.C. ao S.M. Lage, L.C.D. Cavalcante, G. Klingelhöfer, J. Fabris, In-situ57Fe Mössbauer characterization of iron oxides in pigments of a rupestrian painting from the Serra da Capivara National Park, in Brazil, with the backscattering Mössbauer spectrometer MIMOS II, Hyperfine Interact. 237 (2016) 1–7, doi:10.1007/S10751-016-1298-1.

[26] F. Volpi, M. Vagnini, R. Vivani, M. Malagodi, G. Fiocco, Non-invasive identification of red and yellow oxide and sulfide pigments in wall-paintings with portable ER-FTIR spectroscopy, J. Cult. Herit. (2023), doi:10.1016/j.culher.2023.07.019.

[27] A.D. Fovo, S. Mattana, A. Chaban, D.Q. Balbas, J. Lagarto, J. Striová, R. Cicchi, R. Fontana, Fluorescence lifetime phasor analysis and raman spectroscopy of pigmented organic binders and coatings used in artworks, Appl. Sci. (2021), doi:10.3390/app12010179.

[28] L. Beck, H. Rousselière, J. Castaing, A. Durán, M. Lebon, B. Moignard, F. Plassard, First use of portable system coupling X-ray diffraction and X-ray fluorescence for in-situ analysis of prehistoric rock art, Talanta 129 (2014) 459–464, doi:10.1016/j.talanta.2014.04.043.

[29] M.P. Pomiès, M. Menu, C. Vignaud, Red Palaeolithic pigments: natural hematite or heated goethite? Archaeometry 41 (2007) 275–285, doi:10.1111/j.1475-4754.1999.tb00983.x.

[30] F. Lévêque, V. Mathé, Prospection magnétique 3D à haute résolution, Nouv. Archéol. (2015) 19–23, doi:10.4000/nda.2697.

[31] S.D. Mooney, C. Geiss, M.A. Smith, The use of mineral magnetic parameters to characterize archaeological ochres, J. Archaeol. Sci. 30 (2003) 511–523, doi:10.1016/S0305-4403(02)00181-4.

[32] L. Beck, H. Salomon, S. Lahlil, M. Lebon, G.P. Odin, Y. Coquinot, L. Pichon, Non-destructive provenance differentiation of prehistoric pigments by external PIXE, Nucl. Instrum. Methods Phys. Res. Sect. B Beam Interact. Mater. At. 273 (2012) 173–177, doi:10.1016/j.nimb.2011.07.068.

[33] J. Dearing, Environmental Magnetic Susceptibility - Using the Bartington MS2 System, Bartington Instruments, British Library, 1999.

[34] ASD Inc., ViewSpec Pro^{TM} User Manual, (2008).

[35] A. Stevens, L. Ramirez-Lopez, prospectr: miscellaneous functions for processing and sample selection of spectroscopic data, (2024).

[36] M. Witteveen, H.J.C.M. Sterenborg, T.G. van Leeuwen, M.C.G. Aalders, T.J.M. Ruers, A.L. Post, Comparison of preprocessing techniques to reduce nontissue-related variations in hyperspectral reflectance imaging, J. Biomed. Opt. 27 (2022) 106003, doi:10.1117/1.JBO.27.10.106003.

[37] R.F. Kokaly, R.N. Clark, G.A. Swayze, K.E. Livo, T.M. Hoefen, N.C. Pearson, R.A. Wise, W.M. Benzel, H.A. Lowers, R.L. Driscoll, A.J. Klein, USGS spectral library version 7, Reston, VA, 2017. 10.3133/ds1035.

[38] C. Durlet, V. Bichet, J.F. Buoncristiani, Š. Matoušková, P. Sierpień, N. Bondon, Discovery of the world longest known intra-till cave (Jura mountains, France): age and formation processes, Geomorphology 461 (2024) 109319, doi:10.1016/j.geomorph.2024.109319.

[39] T. Holtzapffel, Les Minéraux argileux: préparation, Analyse Diffractométrique Et Détermination, Société géologique du Nord, Villeneuve d'Ascq, France, 1985.

[40] E. Chalmin, E. Sansot, G. Orial, F. Bousta, I. Reiche, Microanalysis and synthesis of calcite. Growth mechanisms on prehistoric paintings in the *Large Cave*, Arcy-sur-Cure (Yonne, France), X-Ray Spectrom. 37 (2008) 424–434, doi:10.1002/xrs.1072.

[41] S. Eyssautier-Chuine, N. Vaillant-Gaveau, M. Gommeaux, C. Thomachot-Schneider, J. Pleck, G. Fronteau, Chlorophyll fluorescence and colorimetric analysis for monitoring the algal development on biocide-treated stone, Open Conf. Proc. J. 7 (2016), doi:10.2174/2210289201607020055.

[42] D. Baffier, M. Girard, Le karst d'Arcy-sur-Cure (Yonne) et ses occupations humaines paléolithiques [The karst of Arcy-sur-Cure (Yonne) and its palaeolithic human occupations], Quaternaire 8 (1997) 245–255, doi:10.3406/quate.1997.1577.

[43] J.C. Liger, Actualité scientifique - Art pariétal : nouvelles découvertes à Arcy-sur-Cure (Yonne), Bull. Société Préhistorique Fr. 87 (1990) 266–269, doi:10.3406/bspf.1990.9446.

[44] M. Girard, J.D. Strich, D. Baffier, D. Molez, Premiers enregistrements photographiques Infra-Rouge dans la Grande Grotte d'Arcy-sur-Cure (Yonne), Bull. Société Préhistorique Fr. 89 (1992) 163–164, doi:10.3406/bspf.1992.9512.

[45] D.E. Critchlow, M.A. Fligner, On distribution-free multiple comparisons in the one-way analysis of variance, Commun. Stat. Theory Methods 20 (1991) 127–139, doi:10.1080/03610929108830487.

[46] J. Fernández-Habas, M. Carriere Cañada, A.M. García Moreno, J.R. Leal-Murillo, M.P. González-Dugo, B. Abellanas Oar, P.J. Gómez-Giráldez, P. Fernández-Rebollo, Estimating pasture quality of Mediterranean grasslands using hyperspectral narrow bands from field spectroscopy by Random Forest and PLS regressions, Comput. Electron. Agric. 192 (2022) 106614, doi:10.1016/j.compag.2021.106614.

[47] G.R. Mahajan, B. Das, B. Gaikwad, D. Murgaonkar, A. Desai, S. Morajkar, K.P. Patel, R.M. Kulkarni, Monitoring properties of the salt-affected soils by multivariate analysis of the visible and near-infrared hyperspectral data, Catena 198 (2021) 105041 (Amst), doi:10.1016/j.catena.2020.105041.

[48] A. Benelli, C. Cevoli, A. Fabbri, S.B. Engelsen, K.M. Sørensen, Precision viticulture: automatic selection of the regions of interest from moving wagon hyperspectral images of grapes for efficient SSC prediction, Smart Agric. Technol. 7 (2024) 100434, doi:10.1016/j.atech.2024.100434.

[49] L. Chiniadis, P. Tamvakis, Rapid detection of soil carbonates by means of NIR spectroscopy, deep learning methods and phase quantification by powder Xray diffraction, (2023). 10.48550/ARXIV.2307.12341.

[50] N. Begum, A. Maiti, D. Chakravarty, B.S. Das, Reflectance spectroscopy based rapid determination of coal quality parameters, Fuel 280 (2020) 118676, doi:10.1016/j.fuel.2020.118676.

[51] T. Sihvonen, Z.S. Duma, H. Haario, S.P. Reinikainen, Spectral profile partial least-squares (SP-PLS): local multivariate pansharpening on spectral profiles, ISPRS Open J. Photogramm. Remote Sens. 10 (2023) 100049, doi:10.1016/j.ophoto.2023.100049.

[52] R.A. Fisher, The use of multiple measurements in taxonomic problems, Ann. Eugen. 7 (1936) 179–188, doi:10.1111/j.1469-1809.1936.tb02137.x.

[53] M.M. Tatsuoka, D.V. Tiedeman, Discriminant analysis, Rev. Educ. Res. 24 (1954) 402–420, doi:10.2307/1169044.

[54] G.J. McLachlan, Discriminant analysis and statistical pattern recognition, J. Wiley and sons, 1992. 10.1002/0471725293.

[55] L.C. Lee, C.Y. Liong, A.A. Jemain, Partial least squares-discriminant analysis (PLS-DA) for classification of high-dimensional (HD) data: a review of contemporary practice strategies and knowledge gaps, Analyst 143 (2018) 3526–3539, doi:10.1039/C8AN00599K.

[56] F. Wang, S. Ma, G. Yan, A PLS-based random forest for NOx emission measurement of power plant, Chemom. Intell. Lab. Syst. 240 (2023) 104926, doi:10.1016/j.chemolab.2023.104926.

[57] Z. Hao, J. Du, B. Nie, F. Yu, R. Yu, W. Xiong, Random forest regression based on partial least squares connect partial least squares and random forest, in: 2016. 10.2991/icaita-16.2016.48.

[58] B. Guo, B. Zhang, Y. Su, D. Zhang, Y. Wang, Y. Bian, L. Suo, X. Guo, H. Bai, Retrieving zinc concentrations in topsoil with reflectance spectroscopy at Opencast Coal Mine sites, Sci. Rep. 11 (2021) 19909, doi:10.1038/s41598-021-99106-1.

[59] W. Zong, G.B. Huang, Y. Chen, Weighted extreme learning machine for imbalance learning, Neurocomputing 101 (2013) 229–242, doi:10.1016/j.neucom.2012.08.010.

[60] B. Lantz, Machine Learning with R: Expert Techniques For Predictive Modeling, Packt Publishing Ltd, 2019.

[61] W. Sun, S. Liu, X. Zhang, Y. Li, Estimation of soil organic matter content using selected spectral subset of hyperspectral data, Geoderma 409 (2022) 115653, doi:10.1016/j.geoderma.2021.115653.

[62] A. Oussama, F. Elabadi, S. Platikanov, F. Kzaiber, R. Tauler, Detection of olive oil adulteration using FT-IR spectroscopy and PLS with variable importance of projection (VIP) Scores, J. Am. Oil Chem. Soc. 89 (2012) 1807–1812, doi:10.1007/s11746-012-2091-1.

[63] X. Fan, S. Tang, G. Li, X. Zhou, Non-invasive detection of protein content in several types of plant feed materials using a hybrid near infrared spectroscopy model, PLoS One 11 (2016) e0163145, doi:10.1371/journal.pone.0163145.

[64] G. Kereszturi, M. Heap, L.N. Schaefer, H. Darmawan, F.M. Deegan, B. Kennedy, J.C. Komorowski, S. Mead, M. Rosas-Carbajal, A. Ryan, V.R. Troll, M. Villeneuve, T.R. Walter, Porosity, strength, and alteration – towards a new volcano stability assessment tool using VNIR-SWIR reflectance spectroscopy, Earth Planet. Sci. Lett. 602 (2023) 117929, doi:10.1016/j.epsl.2022.117929.

[65] I.G. Chong, C.H. Jun, Performance of some variable selection methods when multicollinearity is present, Chemom. Intell. Lab. Syst. 78 (2005) 103–112, doi:10.1016/j.chemolab.2004.12.011.

[66] M. Bevilacqua, R. Bucci, A.D. Magrì, A.L. Magrì, F. Marini, Tracing the origin of extra virgin olive oils by infrared spectroscopy and chemometrics: a case study, Anal. Chim. Acta 717 (2012) 39–51, doi:10.1016/j.aca.2011.12.035.

[67] D.J. Dunlop, Ö. Özdemir, Rock Magnetism: Fundamentals and Frontiers, Cambridge University Press, Cambridge, 1997, doi:10.1017/CBO9780511612794.

[68] R.N. Clark, T.V.V. King, M. Klejwa, G.A. Swayze, N. Vergo, High spectral resolution reflectance spectroscopy of minerals, J. Geophys. Res. Solid. Earth. 95 (1990) 1265312680, doi:10.1029/JB095iB08p12653.

[69] G.R. Hunt, J.W. Salisbury, Visible and near-infrared spectra of minerals and rocks: II. Carbonates, Mod. Geol. 2 (1971) 23–30.

[70] P.L. Harner, M.S. Gilmore, Visible–near infrared spectra of hydrous carbonates, with implications for the detection of carbonates in hyperspectral data of Mars, Icarus 250 (2015) 204–214, doi:10.1016/j.icarus.2014.11.037.

[71] J.L. Bishop, Visible and near-infrared reflectance spectroscopy: laboratory spectra of geologic materials, in: J.F. Bell III, J.L. Bishop, J.E. Moersch (Eds.), Remote Compositional Analysis Techniques for Understanding Spectroscopy, Mineral-

ogy, and Geochemistry of Planetary Surfaces, Cambridge University Press, Cambridge, 2019, pp. 68–101, doi:10.1017/9781316888872.006.

[72] G.R. Hunt, J.W. Salisbury, C. harles J. Lenhoff, Visible and near-infrared spectra of minerals and rocks: III. Oxydes and Hydroxydes, Mod. Geol. 2 (1971) 195–205.

[73] G.R. Rossman, B.L. Ehlmann, Electronic spectra of minerals in the visible and near-infrared regions, in: J.F. Bell III, J.L. Bishop, J.E. Moersch (Eds.), Remote Compositional Analysis Techniques for Understanding Spectroscopy, Mineralogy, and Geochemistry of Planetary Surfaces, Cambridge University Press, Cambridge, 2019, pp. 3–20, doi:10.1017/9781316888872.003.

[74] G.R. Hunt, Spectral signatures of particulate minerals in the visible and near infrared, Geophysics 42 (1977) 501–513, doi:10.1190/1.1440721.

[75] G.R. Hunt, J.W. Salisbury, Visible and near-infrared spectra of minerals and rocks: I. Silicate minerals, Mod. Geol. 2 (1971) 283–300.

[76] S.J. Gaffey, Spectral reflectance of carbonate minerals in the visible and near infrared (0.35–2.55 um): anhydrous carbonate minerals, J. Geophys. Res. Solid Earth 92 (1987) 1429–1440, doi:10.1029/JB092iB02p01429.

[77] S.J. Gaffey, Spectral reflectance of carbonate minerals and rocks in the visible and near infrared (0.35 - 2.55 µm) and its applications in carbonate petrology, 1984.

[78] G.R. Hunt, J.W. Salisbury, Visible and near-infrared spectra of minerals and rocks: XI. Sedimentary rocks, Mod. Geol. 5 (1976) 211–217.

[79] R.N. Clark, in: Spectroscopy of Rocks and Minerals and Principles of Spectroscopy, in: Man. Remote Sens, John Wiley and Sons, New York, 1999, pp. 3–58.

[80] J.K. Crowley, Visible and near-infrared (0.4–2.5 μm) reflectance spectra of Playa evaporite minerals, J. Geophys. Res. Solid Earth 96 (1991) 16231–16240, doi:10.1029/91JB01714.

[81] J.L. Bishop, M.D. Lane, M.D. Dyar, A.J. Brown, Reflectance and emission spectroscopy study of four groups of phyllosilicates: smectites, kaolinite-serpentines, chlorites and micas, Clay Miner. 43 (2008) 35–54, doi:10.1180/claymin.2008.043.1.03.

[82] G.R. Hunt, J.W. Salisbury, C. harles, J. Lenhoff, Visible and near-infrared spectra of minerals and rocks: VI. Additional Silicates, Mod. Geol. 4 (1973) 85–106.